Measurement of the cosmic ray energy spectrum using hybrid events of the Pierre Auger Observatory

G. Cataldi[2], G. Cocciolo[2,3], M. R. Coluccia[1,2], S. D'Amico[2,3] I. De Mitri[1,2], U. Giaccari[1,2,5], G. Marsella[1,2], D. Martello[1,2], L.Perrone[1,2], M. Settimo[1,2,4] and the Pierre Auger Collaboration

[1] Dipartimento di Matematica e Fisica "Ennio De Giorgi", Università del Salento, Italy
[2] Istituto Nazionale di Fisica Nucleare sez. di Lecce, Italy
[3] Dipartimento di Ingegneria dell'Innovazione Università del Salento, Italy
[4] now at the Dept. of Physics, University of Siegen, Germany
[5] now at Universidade Federal do Rio de Janeiro (UFRJ)

1. Introduction

An accurate measurement of the cosmic ray flux above 10^{17} eV is crucial because the features of the energy spectrum of ultra-high energy cosmic rays are intrinsically connected to the origin, nature and propagation of cosmic rays. At the highest energies, above 4×10^{19} eV, a suppression of the flux has been observed by the HiRes experiment [1], the Pierre Auger Observatory [2–5] and the Telescope Array [6]. This suppression is compatible with the predicted Greisen-Zatsepin-Kuz'min (GZK) effect [7], even if other possibilities (e.g. limits in the maximum energy at the source) cannot be excluded. A break in the power law spectrum, named the "ankle", has also been reported around $10^{18.6}$ eV [1–6], this feature being traditionally explained as the intersection of a steep Galactic spectral component with a flatter extragalactic one.

The energy spectrum above 2.5×10^{18} eV has been derived using data from the surface detector array (SD) of the Pierre Auger Observatory [2]. The energy calibration of the SD-array is based on golden hybrid events, i.e. events that can be independently reconstructed from the surface array (SD) and the fluorescence telescopes (FD) [8].

SD data collected between 1 January 2004 and 31 December 2010 have been used for this analysis, which corresponds to an overall SD exposure of 20905 km^2 sr yr. The SD exposure is calculated by integrating the number of active detector stations of the surface array over time. Above 3×10^{18} eV the SD acceptance is saturated regardless of the primary mass and its uncertainty is about 3% [9]. The analysis is limited to events with zenith angle less than 60°. A spectrum measurement using events with larger zenith angle is reported in [10].

The measurement of the energy spectrum has been extended to 10^{18} eV [3–5] using FD events which also triggered at least one station of the surface detector array (hybrid events). Despite the limited number of events, due to the fluorescence detector on-time, the lower energy threshold and the good energy resolution of hybrid events allow us to measure the flux of cosmic rays with the standard array into the energy region where the transition between galactic and extragalactic cosmic rays is expected to occur.

The exposure of the hybrid mode of the Pierre Auger Observatory has been calculated using a time-dependent Monte Carlo simulation. The changing configurations of both fluorescence and surface detectors are taken into account for the determination of the on-time of the hybrid system. Within a time interval of 10 min, the status and efficiency of all detector components of the Observatory, down to the level of the single PMTs of the fluorescence detector, are determined. Moreover, all atmospheric measurements [11] as well as monitoring information are considered and used as input for the simulation. A detailed description of the derivation of hybrid spectrum can be found in [4,5].

In this paper the measurement of the energy spectrum is updated to September 2010 and a method using detailed simulations of the extensive air showers and of the hybrid detector response has been also developed. Hereafter we refer to this approach as "full Monte Carlo". It provides a complete treatment of the shower-to-shower fluctuations and an independent validation of the standard method ("fast simulations") used in [3] and described in detail in [12]. The standard method allows one to simulate a huge amount of events and to apply stricter analysis cuts which reduce the systematic uncertainties on the spectrum measurement. The two approaches

adopted in this paper differ in the EAS and detector simulations and in the selection of events. Their advantages and drawbacks are discussed and the systematic uncertainties related to mass composition, hadronic interaction models and efficiency of the detector are studied.

The Pierre Auger Observatory started collecting data in 2004 [13–15]. The Observatory uses hybrid measurements of air showers recorded by an array of 1660 water Cherenkov surface stations covering an area of 3000 km^2, together with 24 air fluorescence telescopes that observe the development of air showers in the atmosphere above the array during dark nights.

An infill array [16] with half the grid size has been completed and is currently taking data with a threshold of about $3 \cdot 10^{17}$ eV. Moreover, three high-elevation telescopes (HEAT) [17] have begun operation and, together with the infill array in the FOV of the telescopes, will allow us to extend the hybrid measurements further down to 10^{17} eV thus covering with full efficiency the region of the transition from galactic to extra-galactic cosmic rays. The deployment of buried muon detectors (AMIGA) [18] in the infill area is in progress and an extensive R&D program for radio and microwave detection of UHE air showers is under way. The construction of the Auger Engineering Radio Array (AERA) has started [19] and several GHz-antennas are installed and taking data [20].

These extensions and new technologies may enhance the performance and capabilities of the Auger Observatory in Argentina and, in parallel, will explore their potential for a future much larger ground based observatory.

2. Exposure of the hybrid detector

The differential flux $J(E)$ of cosmic rays is defined as the number (dN_{inc}) of events incident on the surface element dS and solid angle $d\Omega$, in the time interval dT and energy bin dE:

$$J(E) = \frac{d^4 N_{inc}}{dE\, dS\, d\Omega\, dt} \simeq \frac{\Delta N_{sel}(E)}{\Delta E} \frac{1}{\mathcal{E}(E)}; \quad (1)$$

where $\Delta N_{sel}(E)$ is the number of selected events in the energy bin centered in E and having a width ΔE, and $\mathcal{E}(E)$ is the exposure of the detector, defined as:

$$\mathcal{E}(E) = \int_T \int_\Omega \int_S \varepsilon(E, t, \theta, \phi, x, y) \, \cos\theta \, dS \, d\Omega \, dt$$

$$(2)$$

ε is the overall efficiency, including detection, reconstruction and selection of the events and the evolution of the detector in the time period T, θ
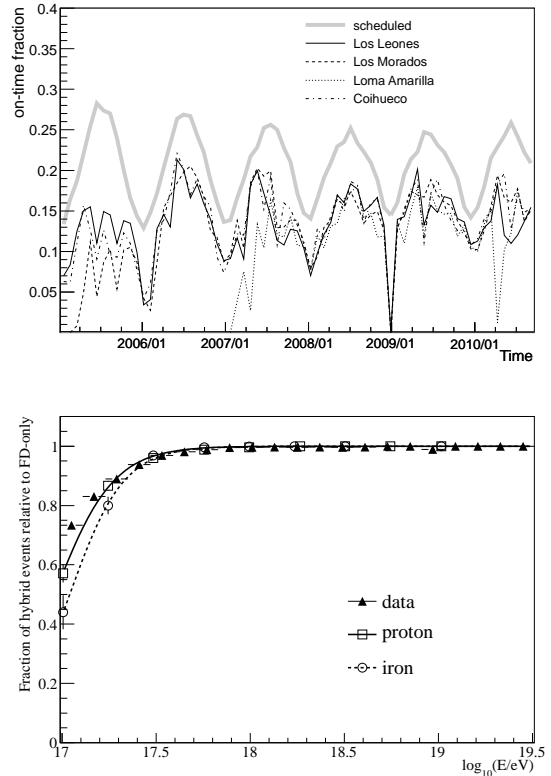
Figure 1. Top: time evolution of the average hybrid on-time fraction for the four FD sites (thin lines). The seasonal modulation, the starting of commissioning phases of the FD and temporary failures are visible. The gray line represents the scheduled data-taking time fraction. It is currently limited to the nights with a moon-fraction lower than 60%. Bottom: relative hybrid trigger efficiency from full Monte Carlo simulation for proton and iron primaries. An estimate of the hybrid trigger efficiency calculated using data is also shown for comparison.

and ϕ are the zenith and azimuth angles respectively, with $0° < \theta < 60°$ and $-180° < \phi < 180°$, Ω and $d\Omega = d\cos\theta\, d\phi$ are the total and differential solid angles, $\cos\theta\, dS$ is the differential projected surface element. The area S encloses the full detector array and is chosen sufficiently large to ensure a negligible trigger efficiency outside of it. During part of the time period analysed here, the Observatory was still under construction. The last FD site was completed at the beginning of 2007 while the last SD station was deployed in June 2008. Also in a steady configuration, the status of each detector may change due to temporary hardware failures, main-

tenance, connections problems, etc. Moreover, the data taking and the trigger efficiency for the fluorescence detection depends on the sky and weather conditions (lunar cycle, brightness of the sky, lightning, wind, cloud coverage and aerosol content). These varying configurations have to be reproduced in simulations for a correct determination of the exposure.

3. On-time calculation

The calculation of the on-time for each FD telescope is derived by taking into account the status of the data acquisition, of the telescopes, pixels, communication system, etc. Details of the on-time and exposure calculations are given in [12]. Since July 2007 a new tool based on the monitoring system [21] has been developed for the on-time calculation, accounting for several terms as discussed below. Before this date, the information on the status of the detector was extracted from a minimum bias datastream which includes sub-threshold FD events, recorded at a rate about 8 times higher than the standard one. The on-time fractions derived using these two tools have been compared in a common time window and they agree to within 3-4%.

As a compromise of accuracy and stability, the on-time of the hybrid detector is calculated in temporal bins, Δt, of 10 minutes. In each time bin t, the detector on-time $f(i,t)$ for the telescope i ($1 \leq i \leq 24$) and FD site s is given by:

$$f(i,t) = \varepsilon_{\text{shutter}}(i,t) \cdot (1 - T^{dead}(i,t)) \cdot \epsilon_{\text{CDAS}}(s,t)$$

where ϵ_{CDAS} refers to the status of the Central Data Acquisition System (CDAS), including connection failures between the SD, the FD and the radio communication towers, $\varepsilon_{\text{shutter}}(i,t)$ gives the fraction of time in which the shutters of each telescope are opened and $T^{dead}(i,t)$ is the cumulative dead time for each telescope divided by Δt. The latter is mostly related to the finite readout speed of the DAQ system, to buffer overflows, vetoed time intervals induced by the operation of the LIDAR system [22] and vetoes from the CDAS in the case of an excessive rate of FD triggers (e.g., because of lightning).

In Fig. 1 (top) the monthly averaged on-time fraction is shown for each FD site (thin lines) as a function of time. The duty-cycle for the FD mainly depends on moon-cycle (the expected mean value is plotted as a gray bold line) and seasonal changes in the daylight and darkness durations. Data taking is currently limited to nights with a moon-fraction smaller than 60%. Compared to the nominal value of darkness, the hybrid detector is in acquisition for about 80-85%

of time, which includes good weather conditions (reasonable brightness of the sky, cloud coverage, wind and no rain) and detector efficiency. In the time interval considered for this analysis, the average overall duty-cycle for the FD is about 14%, over a typical year with stable DAQ conditions.

The status of each SD station is monitored by the CDAS every second. This information is used in simulations to reproduce the actual status of the array. Moreover, time periods with trigger related problems are excluded from the analysis [9]. Systematic uncertainties in the hybrid on-time are estimated to be about 4% based on a cross-check performed using laser shots from the Central Laser Facility (CLF) [23].

4. Time dependent simulations with the full Monte Carlo approach

For an accurate determination of the exposure, all the detector configurations are taken into account by performing detailed time-dependent simulations of the air shower development and of the detector response. Air showers are simulated using the CORSIKA 6.960 [24] Monte Carlo code which provides the longitudinal profile of the showers as well as the secondary particles at the ground (i.e. at the Pierre Auger Observatory altitude). A sample of 70000 CORSIKA showers is used in the present analysis. The air showers have been generated with zenith angle θ distributed as $\sin\theta\cos\theta$ (with $\theta < 65°$), according to the projection on a surface detector of a isotropic flux of cosmic rays, and with energy ranging between 10^{17} eV and $10^{19.5}$ eV, according to a power law spectrum (spectral index $\gamma = -1$) and in intervals of 0.5 in the logarithm of energy. Simulations are performed using QGSJET-II.03 [25], QGSJET-I [26] and Epos-1.99 [27] as hadronic interaction models at high energy and FLUKA [28] at low energy. Moreover, seasonal models of the atmospheric conditions (pressure, temperature and air density) as measured in Malargüe [29] are used in addition to the US standard model [30].

The hybrid detector response is simulated using the Auger Offline software [31]. The FD simulation chain [32] covers the physical processes involved in the fluorescence technique, such as the production of fluorescence and Cherenkov photons in the atmosphere, their propagation to the telescope, the ray-tracing of photons in the Schmidt optics, and the response of the electronics and multi-level trigger. The secondary particles of the shower reaching the ground are injected and traced inside the SD stations and the detector response (including PMTs and electronics) is simulated with Geant4 [33]. The positions of the im-
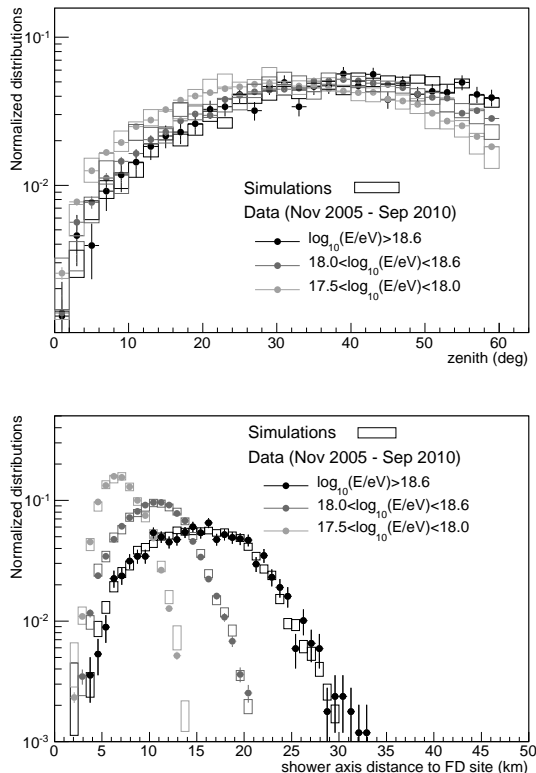
Figure 2. Examples demonstrating the agreement between simulation (boxes) and data (markers) in separate energy bins. For this purpose, the simulations are reweighted according to the spectral index given in [3] and a mixed (50% proton - 50% iron) composition is assumed. The zenith angle and the distance of the shower axis to the FD are shown on the top and bottom, respectively.

pact point of the shower at the ground (hereafter briefly named the "core") are generated uniformly on the surface S including the SD array plus an additional area surrounding the boundaries of the array to take into account events landing outside the array that may still be detected and successfully reconstructed. Its width is energy dependent and its boundaries were defined according to the Lateral Trigger Probability (LTP) functions [34] as boundaries outside of which the trigger probability of a station is negligible (less than 0.5% for events at 60°). Fig. 1 (bottom) shows that every FD event above 10^{18} eV is accompanied by at least one SD station, independently of the mass and direction of the incoming primary particle. For an accurate and unbiased measurement of the energy spectrum, the analysis discussed in this paper is limited to the energy range above

10^{18} eV. A dynamical resampling method has been implemented to optimize the usage of the CORSIKA showers: if an event has no chance of triggering the FD because it is too far from all FD sites, a new core position is generated until the event lands within a (energy dependent) maximum distance from FD, for which the trigger probability is not null [1]. This shower resampling is quite useful at low energy because only events landing within a few kilometers from the FD telescope may have a chance to trigger FD. Within this triggerable region each CORSIKA shower is re-used 7 times, each time with a different core location and a different GPS time (i.e. different detector condition and status), which ensure a negligible degree of correlation. In the time-dependent simulations the actual status of each telescope and SD station, as well as realistic atmospheric conditions (transparency of air, aerosol content, etc.) are taken into account. The detailed simulation of the surface array enables the SD-event trigger to be independently formed, realistically reproducing the full acquisition system.

5. Event selection and data/Monte Carlo comparison

A crucial aspect for the measurement of the energy spectrum is the accurate determination of the shower energy. High quality events with $\theta < 60°$ and with a successful and good reconstruction of the arrival direction and of the longitudinal profile (Gaisser-Hillas fit with a $\chi^2/ndof < 2.5$) are selected. Moreover, we require that the depth, X_{max}, corresponding to the maximum development of the shower, is observed, the fraction of Cherenkov light with respect to the overall signal detected by FD is smaller than 50% and the uncertainty on the reconstructed energy is less than 20%. These selection criteria ensure an average energy resolution of about 10%, almost independent of energy (above $\sim 10^{17.5}$ eV). For a precise energy estimation, the analysis uses only events with available information on the aerosol content [23]. Since clouds may obscure or distort part of the longitudinal profile, the coverage measured by the Lidar system [22] is required to be lower than 25%. A further cut is applied to reduce possible FD trigger effects induced by the systematic uncertainty on the energy scale, estimated to be at the level of 22% [41]. Events are selected if these are landing within a fiducial distance for which the FD trigger efficiency

---

[1] We found that less than 1 out of 10^5 events trigger outside the maximum distance used for the dynamical resampling, even considering realistic atmospheric conditions and different fluorescence yield models.

is flat within 5% when shifting the energy scale by its systematic uncertainty. The reliability of the quality criteria are checked by comparing the distributions of several observables taken from both data and Monte Carlo. Two examples are given in Fig. 2 for the zenith angle (top) and the shower axis distance to the FD (bottom). In both plots, the comparison is performed in three separate energy intervals and simulations are reweighted according to the spectral indices obtained in [3]. The agreement between data (markers) and simulations (lines) is fairly good for both observables in the three energy ranges.

The hybrid exposure, given by equation 2, is shown in Fig. 3 for proton and iron primaries. A mass composition dependence is visible, particularly at low energies. Indeed, at these energies iron primaries, developing higher in the atmosphere, have a smaller probability of being detected and being well observed in the FD field of view (FOV) than protons. At higher energies, events far away from an FD are mainly selected. For these events the lower bound of the FD field of view disfavours deep (*i.e.* proton induced) showers. In Fig. 3 (bottom), the ratio of the exposure of each pure composition relative to a mixed one (50% proton - 50% iron) is given as a function of energy. At energies above 10^{18} eV, the difference is less than $\sim 10\%$ depending on the energy and it rapidly increases at lower energy. As a consequence of this dependence, and given the lack of accurate knowledge of the nature of primary cosmic rays in this energy range, a mass-independent measurement of the energy spectrum cannot be performed. Estimates of the energy spectrum can be derived assuming a pure proton and a pure iron composition, which provides a confidence region (see section 8) in which we expect the spectrum to be confined if the cosmic ray flux is dominated by nuclear primaries. Photons as primary particles at these energies are strongly constrained [35,36].

6. Exposure calculation with fast simulations

As discussed in the previous section, the limited field of view of the fluorescence detector and the requirement of observing the shower maximum may introduce a different selection efficiency for different primary masses. To reduce the impact of mass composition on the hybrid exposure, a dedicated analysis has been performed by defining a geometrical volume which guarantees comparable selection efficiency to all nuclear primaries. For a given energy and event geometry, this volume is defined by setting the lower and upper bound-
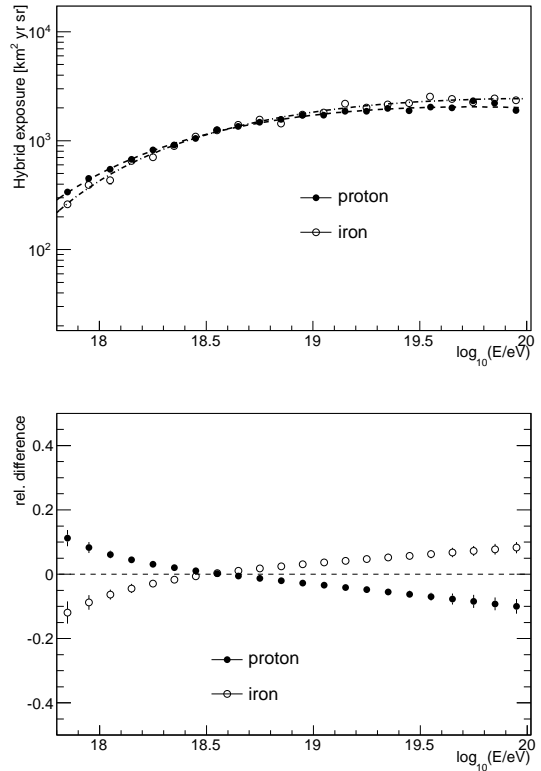
Figure 3. Top: hybrid exposure for proton (filled markers) and iron (empty markers) as a function of energy. Bottom: difference in the exposure for proton and iron, relative to that for a mixed (50% proton - 50% iron) composition.

aries (expressed in atmospheric depth) of the FD field of view. This "fiducial FOV cut" is applied in addition to the quality selection criteria described in the previous section and it reduces the primary mass dependence to 8% (1%) at 10^{18} eV (above 10^{19} eV) [12]. Moreover the cut on the FD fiducial distance, introduced in section 5, is applied here more strictly, requiring an FD efficiency larger than 99% independently of a shift of $\pm$ 22% on the energy scale. The benefit of this cut is demonstrated in Fig. 4, top. The lines show the relative difference between the exposure with $\pm 22\%$ shifted energy and the nominal value, for two definitions of the fiducial distance cut (dashed and dotted) and if the cut is not applied (solid).

Because of the strict selection and the demanding resources for a high statistics sample of full Monte Carlo simulations, a fast and simplified approach has been adopted to produce a large sample of simulations in a reasonable computational time. This method uses the CONEX [37] code to

6
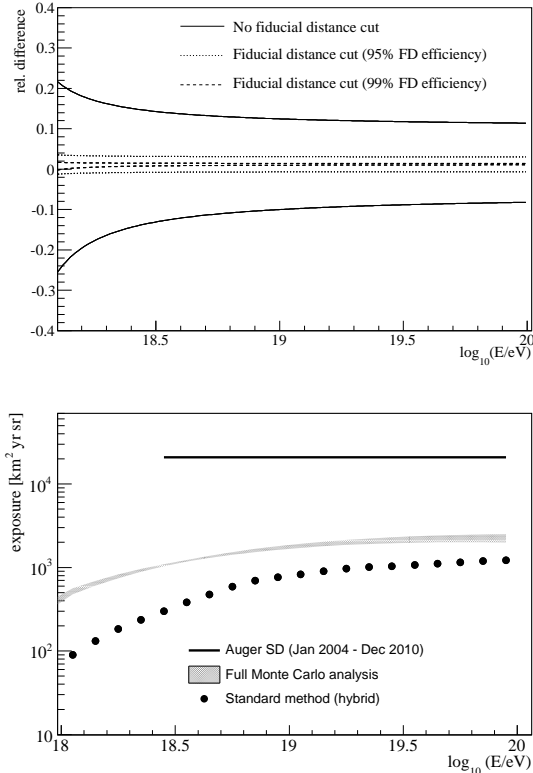
Figure 4. Top: relative difference between the hybrid exposure with a $\pm$ 22% shift and the nominal value (solid lines). Fiducial distance cuts are designed to reduce this effect requiring an efficiency higher than 95% (dotted line) and higher than 99% (dashed line). Bottom: exposure calculated between November 2005 and September 2010 for the hybrid detector. The mixed composition assumption is plotted for the standard method, based on fast simulations and on an analysis designed to reduce the systematic uncertainties due to mass composition. For the full Monte Carlo approach, a shaded region delimited by the pure proton and pure iron cases is shown. Its higher value results from the different selection criteria (see text). The exposure for the SD array (line), between January 2004 and December 2010, is also given.

simulate the air shower profile by a Monte Carlo generation of the first interactions and then a numerical solution of the cascade equations. This EAS generator is extremely fast and reproduces accurately the longitudinal profile including its shower-to-shower fluctuations [37,38]. However it has the drawback of not providing the distribution of secondary particles at the ground and,

consequently, the response of the detector cannot be directly simulated. The SD trigger is thus extracted using the Lateral Trigger Probability (LTP) functions, which parametrize the trigger probability of each SD station as a function of its distance to the shower axis, and of the energy and arrival direction of the primary cosmic ray. Even though the probability of having at least one station for each FD event is unity above 10^{18} eV, this procedure may be relevant for low energy and inclined events. The SD timing information needed in the hybrid reconstruction mode is modelled with an NKG-like [39,40] function for the lateral distribution of the air showers. The validity of this assumption has been verified in [12].

The FD response is fully simulated with the approach and on-time tools described above. The hybrid exposure calculation based on the "fast simulation" and on the corresponding selection criteria, is the same used in [3,4] for previous spectrum measurements. For this reason, the approach discussed in this section is also referred to as the "standard method". The exposure is shown in Fig. 4 (bottom) for a mixed composition (filled dots) of 50% proton and 50% iron primaries. This assumption, especially for energies above 10^{19} eV, is well justified because of the reduced mass composition dependence of the exposure. The residual difference between proton and iron, for the standard method, is accounted as systematic uncertainty (see section 7). For comparison, the exposure derived in section 4 (full Monte Carlo approach) is here plotted as a band delimited by the pure proton and pure iron assumptions. As a consequence of the less strict cuts, this exposure is significantly higher, especially at low energies. However the systematic uncertainty related to mass dependence is higher. The tighter analysis cuts introduced in this section have also been applied to full Monte Carlo approach and the derived exposure is in agreement with the one from the fast simulation. This check further validates the reliability of the standard method. As reference, the exposure derived using the SD-only array, valid for energies above $\sim 10^{18}$ eV, is shown in Fig. 4 (bottom) until December 2010. Details on the SD exposure are given in [9,4].

7. Systematic uncertainties

For the standard method, the overall systematic uncertainty in the exposure calculations has been estimated as 10% (6%) at 10^{18} eV ($> 10^{19}$ eV). It includes the contributions listed below and discussed in detail in [12]. The uncertainties in mass composition (8% at 10^{18} eV and

1% above 10^{19} eV) and in the on-time calculation ($\sim4\%$) have been discussed in the previous sections. As a result of the checks with CLF laser shots and between SD data and the Monte Carlo simulations, the exposure has been reduced by 8% to account for lost events and an upper limit to the remaining systematic uncertainty of 5% has been derived. Different hadronic interaction models used for simulations may produce different predicted properties of the showers and consequently different trigger and selection efficiency. The impact on the exposure has been studied in [12] using QGSJETII-03 and Sibyll 2.1 [42] as hadronic interaction models and the average effect is lower than 2% over the full energy range. Furthermore, an additional uncertainty of about 2% is quoted due to the choice of the index of the input spectra used in simulations.

For the full Monte Carlo approach, the overall systematics are larger, dominated by the uncertainty on the mass composition. This is below than 10% in the energy range above 10^{18} eV. The systematic uncertainties on common tools (*i.e.* on-time) and based on general cross-checks (laser shots and data/MC comparison) have been considered following the standard method. The dependence of the exposure on the hadronic interaction models has been checked using QGSJET-I and Epos-1.99 as additional models for the EAS generation. An impact of about 2% has been found over the full energy range and assuming a mixed composition. Since the choice of different atmospheric profile may also influence the shower development, EAS simulations have been performed using realistic Malargüe seasonal models and the US standard profile models, implemented in CORSIKA. The final impact on the exposure is smaller than 2%. Compared to the standard method, an additional contribution of less than 4% (Fig. 4, top) has to be considered because of the looser FD fiducial distance cut used in the full Monte Carlo analysis (see section 4). This contribution includes the systematic uncertainty related to different choices of fluorescence yield that may change the maximum triggerable volumes at given energies. This check only refers to trigger and selection efficiency, since a consistent fluorescence yield is used in the simulation and the reconstruction phases. The impact of a different fluorescence yield on data reconstruction is included in the uncertainty on the energy scale and will be discussed in the next section. The overall systematic uncertainty in the exposure does not exceed $\sim$ 13% above 10^{18} eV for the full Monte Carlo approach. A discussion of the energy region below 10^{18} eV is given in the appendix.

8. Energy spectrum

The flux of cosmic rays as a function of energy is shown in Fig. 5 and compared to the one derived from the full Monte Carlo approach (empty squares with gray boxes). To emphasize their features, the two energy spectra are multiplied by an E^3 factor. In the full Monte Carlo approach,
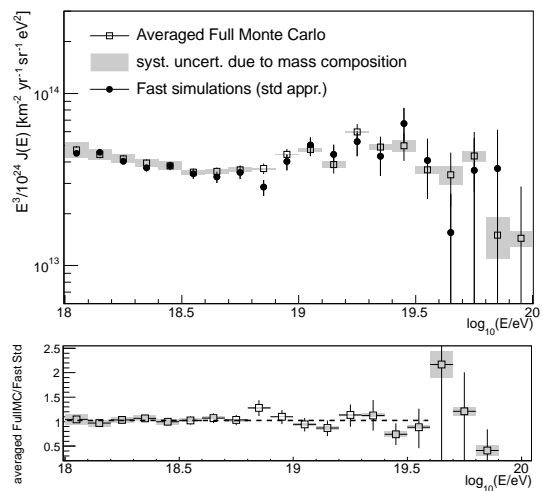
Figure 5. Comparison between the spectra measured using the hybrid exposure calculated with the fast simulation (dots) and the full Monte Carlo approach (empty squares). Because of the looser cuts used for the full Monte Carlo, an averaged spectrum is shown, with the systematic uncertainties due to mass composition (dark gray boxes). Bottom panel: ratio between the two spectra.

because of the systematic uncertainties and the lack of knowledge of the mass composition of cosmic rays in this energy range, the spectrum has been derived using the two extreme assumptions of pure proton and pure iron composition. The missing energy [45] assigned to data is chosen according to the primary mass. These two assumptions delimit a confidence region (gray boxes) in which the all-particle spectrum is expected to be found. The relative difference between the spectra derived with the two approaches is shown in the bottom panel. They differ by less than a few percent and they are compatible within the uncertainties. This good agreement between the two approaches, which are quite different concerning

data sample, cuts and methods, is a nice confirmation for the resulting flux spectrum.

The main source of systematic uncertainty on the energy spectrum is the 22% on the energy scale. In particular, the largest contribution (14%) is given by the absolute scale of the fluorescence yield [43]. The absolute calibration of the fluorescence telescope contributes about 9%. An additional uncertainty of about 5% is due to the measurement of atmospheric pressure, humidity and temperature and 4%-8% (depending on energy) is related to the attenuation of the light. Uncertainties of the lateral width of the shower image and other steps in the hybrid reconstruction method contribute about 9.5% to the total uncertainty in the measured energy. The fraction of energy of the primary particle that is carried by muons and neutrinos has been calculated based on air shower simulations and goes from about 14% at 10^{18} eV to about 10% at 10^{19} eV. The systematic uncertainty depending on the choice of models and mass composition, is about 4%. Indirect methods [44] of determining the energy scale, which do not involve the fluorescence detector calibration, seem to indicate an energy normalisation that is higher than the one used here by an amount comparable to the systematic uncertainty (22%) given above.

The energy spectrum derived from hybrid data has been combined with the one obtained from surface detector data using a maximum likelihood method. Since the surface detector energy estimator is calibrated with hybrid events, the two spectra have the same systematic uncertainty in the energy scale. On the other hand, the normalisation uncertainties are independent. They are taken as 6% for the SD and 10% (6%) for the hybrid flux at 10^{18} eV ($¿ 10^{18}$ eV). These normalisation uncertainties are used as additional constraints in the combination.

The characteristic features of the combined spectrum have been quantified with three power laws with free breaks between them (dashed line in Fig. 6) and with two power laws plus a smoothly changing function (solid line). The latter function is given by:

$$J(E; E > E_{\mathrm{ankle}}) \quad \propto \quad E^{-\gamma_2} \frac{1}{1 + \exp\left(\frac{\lg E - \lg E_{\frac{1}{2}}}{\lg W_c}\right)},$$

where $E_{\frac{1}{2}}$ is the energy at which the flux has fallen to one half of the value of the power-law extrapolation and W_c parametrizes the width of the transition region. The hypothesis that the power law above the ankle continues to highest energies with the spectral index γ_2 can be rejected with more than $20\,\sigma$. The derived parameters with their sta-
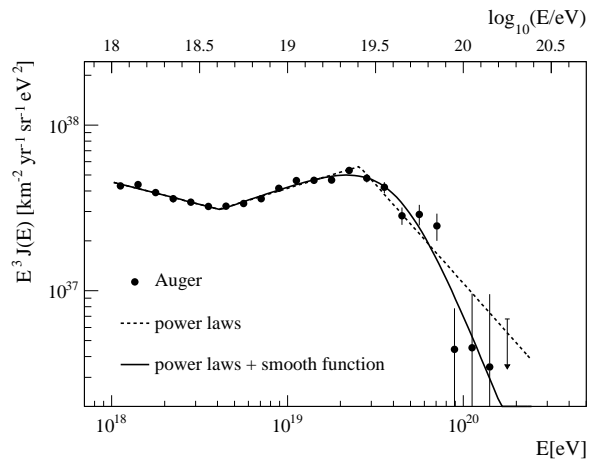
Figure 6. The combined Auger energy spectrum. A fit with three power law functions (dashed) and one with two power laws plus a smooth function (solid line) are superimposed. Only statistical uncertainties are shown. The systematic uncertainty on the energy scale is 22%.

tistical uncertainties are given in Table 1. Both, the ankle and suppression of the flux at higher energies are clearly visible.

parameter	broken power laws	power laws + smooth function
$\gamma_1 (E < E_{\mathrm{ankle}})$	3.27 ± 0.02	3.27 ± 0.01
$\lg(E_{\mathrm{ankle}}/\mathrm{eV})$	18.61 ± 0.01	18.62 ± 0.01
$\gamma_2 (E > E_{\mathrm{ankle}})$	2.68 ± 0.01	2.63 ± 0.02
$\lg(E_{\mathrm{break}}/\mathrm{eV})$	19.41 ± 0.02	
$\gamma_3 (E > E_{\mathrm{break}})$	4.2 ± 0.1	
$\lg(E_{\frac{1}{2}}/\mathrm{eV})$		19.63 ± 0.02
$\lg(W_c/\mathrm{eV})$		0.15 ± 0.02
χ^2/ndof	$37.8/16 = 2.4$	$33.7/16 = 2.1$

Table 1
Fit parameters with their statistical uncertainties

The spectrum can be compared to astrophysical models and can be described by both a proton and heavy-dominated composition at the highest energies. Thus, measurements of the composition are needed to discriminate between various astrophysical models.

REFERENCES

1. R. Abbasi *et al.*, HiRes Collaboration, Phys. Rev. Lett. **100**, (2008) 101101.

2. The Pierre Auger Collaboration, Physical Review Letters **101**, (2008) 061101.

3. The Pierre Auger Collaboration, Physics Letters **B 685**, (2010) 239.

4. F. Salamida, for the Pierre Auger Collaboration, Proc. 32nd ICRC, Beijing, China (2011), arXiv:1107.4809.

5. M. Settimo for the Pierre Auger Collaboration, Eur. Phys. J. Plus **127** (2012) 87.

6. Telescope Array Collaboration, submitted to PRL, arXiv:1205.5067v1.

7. K. Greisen, Phys. Rev. Lett.**16**, (1966) 748. G. T. Zatsepin, V.A. Kuz'min, Pis'ma Zh. Eksp. Teor. Fiz., **4**(3), (1966) 114.

8. R. Pesce for the Pierre Auger Collaboration, Proc. 32nd ICRC, Beijing, China (2011)arXiv:1107.4809.

9. The Pierre Auger Collaboration, Nucl. Instrum. Meth. **A613** (2010) 29.

10. H. Dembinski, for the Pierre Auger Collaboration, Proc. 32nd ICRC, Beijing, China (2011), arXiv:1107.4809.

11. K. Louedec, for the Pierre Auger Collaboration, Proc. 32nd ICRC, Beijing, China (2011), arXiv:1107.4806.

12. The Pierre Auger Collaboration, Astropart. Phys., **34**, (2011) 368.

13. The Pierre Auger Collaboration, Nucl. Instrum. Meth. **A 523** (2004) 50.

14. The Pierre Auger Collaboration, Nucl. Instrum. Meth. **A 620** (2010) 227.

15. I. Allekotte et al. for the Pierre Auger Collaboration, Nucl. Instrum. Meth. **A 586** (2008) 409.

16. I. Mariş for the Pierre Auger Collaboration, Proc. 32nd ICRC, Beijing, China (2011), arXiv:1107.4809.

17. H-J.Mathes, for the Pierre Auger Collaboration, Proc. 32nd ICRC, Beijing, China (2011), arXiv:1107.4807.

18. F. Sanchez, for the Pierre Auger Collaboration, Proc. 32nd ICRC, Beijing, China (2011), arXiv:1107.4807.

19. The Pierre Auger Collaboration, JINST **7** (2012) P11023.

20. P. Facal for the Pierre Auger Collaboration, UHECR-2012, CERN, February 13rd-17th, (2012).

21. J. Rautenberg [Pierre Auger Collaboration], Proceedings of 31th Int. Cosmic Ray Conf. (ICRC 2009), arXiv:0906.2358.

22. S. Y. BenZvi *et al.*, Nucl. Instr. Meth. Phys. Res, **A 574**, (2007) 171.

23. B. Fick *et al.*, J. Instrum. (JINST) **1**, (2006) 11003.

24. D. Heck *et al.*,*"CORSIKA: A Monte Carlo Code to Simulate Extensive Air Showers"*, Report FZKA, **6019**, (1998).

25. S. Ostapchenko, Phys. Lett., **B 636**(1), (2006) 40-45.

26. N. N. Kalmykov and S. Ostapchenko, Sov. J. Nucl. Phys., **50**(2), (1989) 315.

27. T. Pierog, K. Werner, Phys. Rev. Lett. **101**, (2008) 171101.

28. A. Fassò *et al.*, CERN-2005-10 (2005) INFN/TC_05/11, SLAC-R-773.

29. B. Keilhauer *et al.*, Astropart. Phys. 22 (2004), 249.

30. J. Linsley, private communication by M. Hillas (1988).

31. S. Argirò *et al.*, Nuclear Instruments and Methods in Physics Research, **A 580**, (2007) 1485.

32. L. Prado *et al.*, Nucl. Instrum. Meth., **A545** (2005), 632.

33. S. Agostinelli *et al.*, Nuclear Instruments and Methods in Physics Research, **A 506**, (2003) 250; IEEE Transactions on Nuclear Science, **53**(1), (2006) 270.

34. The Pierre Auger Collaboration, Astropart. Phys., **35**, (2011) 266.

35. M. Settimo, for the Pierre Auger Collaboration, Proceedings of 32th Int. Cosmic Ray Conf. (ICRC 2011), arXiv:1107.4805.

36. The Pierre Auger Collaboration, Astropart. Phys., **29**(4), (2008) 243.

37. T. Bergmann *et al.*, Astropart. Phys. **26**, (2007) 420.

38. T. Pierog, *et al.*, Proceedings of the 30th Int. Cosmic Ray Conf. (ICRC 2007).

39. K. Kamata, J. Nishimura, Prog. Theoret. Phys. Suppl. **6**, (1958) 93.

40. K. Greisen, Prog. Cosmic Rays Phys. III, (1965) 26.

41. C. Di Giulio, for the Pierre Auger Collaboration, Proceedings of 31st Int. Cosmic Ray Conf. (ICRC 2009), arXiv:0906.2189.

42. E.-J. Ahn, R. Engel, T.K. Gaisser, P. Lipari, T. Stanev, Phys. Rev.**D 80**, (2009) 094003.

43. M. Nagano, K. Kobayakawa, N. Sakaki, and K. Ando, Astropart. Phys. **20**, (2003) 293.

44. A. Castellina, for the Pierre Auger Collaboration, Proceedings of 31th Int. Cosmic Ray Conf. (ICRC 2009), arXiv:0906.2319.

45. H. M. J. Barbosa, F. Catalani, J.A. Chinellato, C. Dobrigkeit, Astropart. Phys.**22**, (2004) 159.